PCCP

ROYAL SOCIETY OF CHEMISTRY

PAPER

View Article Online
View Journal

Cite this: DOI: 10.1039/d5cp03612g

Investigations on the field dependency of proton and charge transfer kinetics in atmospheric pressure corona discharge sources

Christoph Schaefer, *† Alexander Haack, *† Charlotte Hellwig, Jannik Wuttke and Stefan Zimmermann

Proton and charge transfer are two commonly observed reaction mechanisms in the chemical ionisation of neutral analytes in mass spectrometry and ion mobility spectrometry. While those reactions show a strong influence on effective temperature, influenced by the applied electric field strengths, a detailed understanding of the underlying mechanisms under such conditions is still lacking. Using a high kinetic energy ion mobility spectrometer, we examine the reaction dynamics of proton transfer from $H_3O^+(H_2O)_n$ and charge transfer from $NO^+(H_2O)_m$ to the model analytes benzene, toluene, and *p*-xylene experimentally and compare this to quantum chemical modelling of the ionisation processes over a wide range of effective temperatures. Our findings underline that the reduced field strength (*E*/*N*) significantly affects the ion-neutral reactions due to its influence on effective temperature, leading to significant changes in reaction rate coefficients. Particularly when ionisation proceeds *via* H_3O^+ and NO^+, the reaction rate coefficients approach the association rate in most cases. However, hydration of the reactant ions can slow down the reaction since the dynamics of intermediate reaction complexes need to be considered, as these can introduce additional internal barriers. Especially when subjected to high *E*/*N*, those reaction complexes can either dissociate back to the reactants or towards the products, with the branching ratio determined by the kinetics of both reaction paths. Particularly when the ionisation energies or proton affinities of the neutral precursor of the reactant ion and the neutral analyte are similar, this product branching can introduce deviations between the experimentally observed reaction rates and the association rates.

Received 18th September 2025,
Accepted 9th January 2026

DOI: 10.1039/d5cp03612g

rsc.li/pccp

Introduction

Mass spectrometers (MS) and ion mobility spectrometers (IMS) analyse gas-phase ions based on their characteristic properties such as the mass-to-charge ratio, *m*/*z*, and the reduced ion mobility, K_0, respectively. Since only charged particles are analysed, effective ionisation of neutral analytes is a critical first step. A comprehensive understanding of the underlying ionisation processes is therefore essential for interpreting analyte behaviour and instruments' performance, as well as for optimising the instruments to achieve effective ionisation in practical applications.

Many stand-alone IMS and chemical ionisation MS (CI-MS), such as proton transfer reaction mass spectrometers (PTR-MS)[1,2] or selected ion flow tube mass spectrometers (SIFT-MS),[3] use ion-neutral reactions for chemical ionisation. Focusing on positive ionisation, initially formed reactant ions such as H_3O^+, NO^+, $O_2^{+\bullet}$ and occasionally NH_4^+ are commonly used to ionise neutral analytes *via* proton transfer (PT) or charge transfer (CT), forming protonated monomers or radical cations.[4–6] A detailed understanding of these ion-neutral reactions requires both accurate identification of product ions and investigation of the reaction kinetics.

In the simplest case, the ionisation proceeds *via* the following reaction scheme:

$$RI^+ + A \xrightarrow{k_1} [RI + A]^+ \quad (1)$$

$$[RI + A]^+ \xrightarrow{k_{-1}} RI^+ + A \quad (2)$$

$$[RI + A]^+ \xrightarrow{k_2} RI + A^+ \quad (3)$$

I.e., the initial step is the formation of an intermediate reaction complex $[RI + A]^+$ by association of the reactant ion RI^+ and neutral analyte A, which can then either dissociate back to the reactants or towards the ionised analyte and neutralised reactant ion. Assuming the reaction complex is short-lived, the

Leibniz University Hannover, Institute of Electrical Engineering and Measurement Technology, Department of Sensors and Measurement Technology, Appelstr. 9A, 30167 Hannover, Germany. E-mail: schaefer@geml.uni-hannover.de, haack@geml.uni-hannover.de

† The authors contributed equally to this work.

first-order total rate coefficient for the formation of $[A^+]$ (see Section S2 in the SI) is:

$$k_{tot} = \frac{k_2 k_1[A]}{k_{-1} + k_2} = k_{obs}[A] \quad (4)$$

This rate coefficient can be further simplified in case of two limiting cases: if the reaction back to the reactants is strongly favoured, *i.e.*, $k_2 \ll k_{-1}$, we obtain a total rate that is equal to the decomposition rate of the reaction complex towards the products times the equilibrium constant for the initial association of the reaction complex.

$$k_{tot} \approx k_{lim\,1} = k_2 \frac{k_1[A]}{k_{-1}} = k_2 K_{ass} \quad (5)$$

Conversely, if $k_2 \gg k_{-1}$, *i.e.*, the decomposition of the reaction complex towards the products is rapid compared to the back reaction, the total rate becomes equivalent to the association rate:

$$k_{tot} \approx k_{lim2} = k_1[A] \quad (6)$$

Note that in limit 2, every association reaction leads to analyte ionisation, whereas in limit 1 only the small portion of reaction complex existing in equilibrium (described by K_{ass}) can react to the products with the rate coefficient k_2. Thus, ideal ionisation efficiency would be obtained in the limit 2 case, which effectively describes the association limit.

At ambient temperature, these ion-neutral reactions are well characterised, supported by extensive kinetic libraries of reaction rate coefficients, primarily obtained using SIFT-MS.[3] However, at high reduced electric field strengths (defined as the ratio of the electric field and the neutral particle density, E/N), ions gain substantial energy from the electric fields, leading to high effective temperatures and significant ion heating.[7] This ion heating can alter the ion-neutral interaction dynamics through changes in their relative velocities (and thus collision rates), but also through destabilising loosely bound ion-neutral clusters, *e.g.* the reaction complexes $[RI + A]^+$ necessary for proton and charge transfer, or hydrates of the reactant ions $M^+(H_2O)_n$ which determine their proton or charge transfer efficiencies.[8–11] Thus, E/N can have a substantial effect on the reaction rate coefficients of proton and charge transfer reaction. Depending on the analyte studied, high E/N may even induce field-induced fragmentation of product ions.[12–14] Despite the importance of such effects, detailed understanding of field-dependent dynamic effects and interactions are still lacking. The same applies to comprehensive libraries of reaction rate coefficients at elevated E/N.

A suitable instrumental platform for generating such data is the high kinetic energy ion mobility spectrometer (HiKE-IMS),[15] operated at reduced pressure of 5–40 mbar, resulting in comparatively low neutral particle densities. This enables variation of reduced field strengths in a wide range from 20 to 120 Td in both the reaction region, where the ion-neutral reactions occur, and the drift region, where separation based on ion mobility takes place. Hence, by varying E/N, HiKE-IMS offers controlling ion chemistry and ion separation. The reactant ions can reach high effective temperatures, exceeding 1500 K,[16] significantly affecting ion chemistry and making HiKE-IMS well-suited for detailed studies on ion-neutral reactions. However, the current instrumentation is not yet optimised for detailed studies on reaction kinetics as previous studies on the influence of E/N and water concentration on product ion formation in HiKE-IMS[17–20] have revealed that reactant ion composition strongly depends on these parameters as well. For instance, NO^+ and $O_2^{+\bullet}$ are typically present only at high reduced field strengths and low water concentrations, as they can form hydrates at low E/N, particularly at high water concentrations, eventually leading to the formation of $H_3O^+(H_2O)_n$.[9,21–26] Changes in the relative intensities of reactant ions can complicate a detailed investigation and understanding of effects of E/N on ion-neutral reactions. Furthermore, in the HiKE-IMS setup used before, analytes are evacuated near the corona discharge ion source, which initiates reactant ion formation. This results in neutral analytes reacting not only with target reactant ions but also with transient species formed during ion formation, complicating data interpretation for detailed understanding of the underlying ion-neutral reactions. To address these challenges, a new ion source is introduced in this work. With the modified instrumental setup, effects that complicate the determination of reaction rate coefficients should be minimised.

Using this optimised instrumental platform, the primary aim of this work is to investigate how field-dependent effects influence the reaction kinetics of proton and charge transfer. Specifically, the study focuses on reaction kinetics for proton transfer from $H_3O^+(H_2O)_n$ and charge transfer from $NO^+(H_2O)_m$ to the model analytes benzene, toluene, and *p*-xylene. These three model analytes are considered suitable since previous work has identified the formed product ions,[19] and the experiments in this work can complement the previous study with investigating their reaction kinetics. Moreover, these model analytes primarily form their protonated monomers and radical cations, and particularly no fragments, and are therefore very well suited for these investigations. Hence, this work aims to provide a comprehensive understanding of how E/N influences ion-neutral reactions.

Experimental

Materials and methods

Development of ion source. To allow for determination of reaction rate coefficients of proton and charge transfer depending on E/N, a modified instrumental setup is introduced in this work, discussed in detail in Section S1, including spatial separation of reactant ion formation and neutral analyte ionisation. With this modified setup, reactant ions will be selectively generated in the developed ion source from Fig. 1, meaning that only one reactant ion species is formed in high purity and then transferred to the reaction region. Reactant ion formation is initiated by applying a high voltage between a needle and a hollow electrode, leading to a glow discharge. The discharge current is limited by a serial resistor. The ion source is constructed from four individual PCBs,[27,28] one on each side, similar to previous PCB-based IMS designs, bonded together to

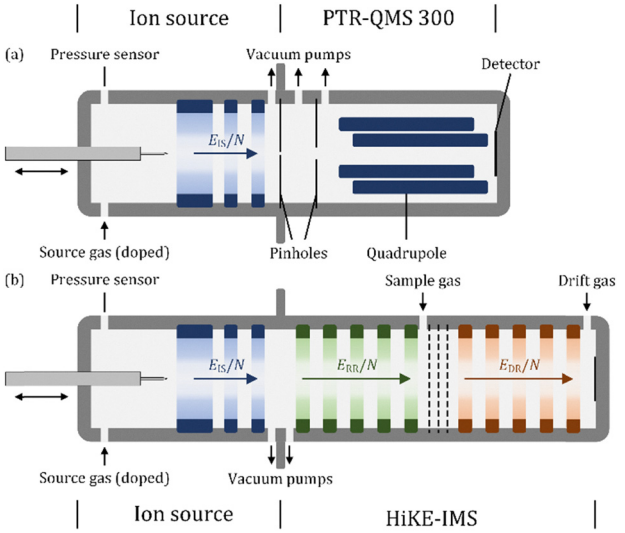

Fig. 1 Schematic setup of (a) a coupling of the developed ion source and the PTR-QMS 300 with an intermediate pressure stage, and (b) a coupling of the developed ion source with a HiKE-IMS. The ion source allows for selecting ion species in high purity. In both configurations, the ion source itself consists of a needle electrode, a hollow electrode and drift rings. The detailed operating parameters are summarised in Tables S1–S3.

maintain the operating pressure. Applying a voltage between the hollow electrode and the end of the ion source establishes a reduced field strength E/N. Inside the ion source, parameters such as this E/N value, along with the neutral gas composition, will be optimised to ensure that the reaction system reaches chemical equilibrium by the end of the ion source, with only the selected reactant ion species present, *e.g.*, H_3O^+ or NO^+. Hence, the ion source selectively provides only a single reactant ion species. Reactant ions will then ionise neutral analytes in the reaction region through proton or charge transfer. A mass flow controller (F-200DC-ABD, Bronkhorst Nord, Germany) supplies a doped source gas to select specific reactant ion species with a constant flow rate of 12 mL min^{-1} (related to 1013.25 hPa and 293.15 K). The ion source is evacuated by a diaphragm pump (MVP 040-2, Pfeiffer Vacuum, Germany), with a capacitive pressure gauge (CMR 362, Pfeiffer Vacuum, Germany) monitoring the operating pressure.

Note that PTR-MS[4,5] and SIFT-MS[29] can also employ modified ion sources to selectively provide only a single reactant ion species for analyte ionisation. Both these instruments are capable of investigating the underlying ion-neutral reactions.[3,12,30] While PTR-MS analyse ion-neutral reactions depending on E/N, SIFT-MS are usually operated at ambient temperature without any electric field along the drift tube. Modern SIFT-MS instruments operate at elevated temperatures (120 °C) and apply electric fields at the inlet and outlet of the flow tube to improve ion transmission. A variant of the technique, selected ion flow-drift tube MS (SIFDT-MS),[31] uses a homogeneous reduced field strength up to 50 Td, throughout the entire drift tube. Similar to SIFDT-MS, the homogeneous electric field in the drift region of the HiKE-IMS allows direct extraction of drift velocities from the arrival time distributions. These allow for calculation of effective temperatures using the Wannier equation.[7] Because this effective temperature captures both the gas temperature and the influence of the reduced field strength, it provides a more comprehensive measure of ion-neutral collision energy than E/N alone. Since the theory on chemical reaction kinetics are based on temperature as the central quantity, HiKE-IMS can potentially provide a deeper insight into ion behaviour, as it covers a wider range of E/N and thus effective temperatures compared to other techniques.

Two different self-built setups will be employed in this study. First, the developed ion source was coupled to the inlet pinhole of a quadrupole mass spectrometer (PTR-QMS 300, Ionicon Analytik, Austria) to reliably identify the formed reactant ions and assess their purity (see Section S1). For this configuration, the original reaction region and ion source of the PTR-QMS 300 were replaced by the developed ion source depicted in Fig. 1. Here, the ions generated in the glow discharge are transported towards the outlet of the ion source by the defined reduced field strength E/N and are transferred through the existing differential-pumping interface of the PTR-QMS 300 without further modification. After passing the intermediate pressure stage, the ions enter the quadrupole mass filter, which mass-selectively transmits the reactant ions to the detector for m/z identification. For all measurements in this configuration, PTR-QMS 300 was operated in full-scan mode.

Following this characterisation, the ion source was connected to a HiKE-IMS, consisting of a reaction region and drift region, to study the reaction kinetics of proton transfer with $H_3O^+(H_2O)_n$ and charge transfer with $NO^+(H_2O)_m$. Similar to previously described HiKE-IMS configurations,[32] the reactant and drift region consist of alternating stainless-steel electrodes separated by polyether ether ketone (PEEK) insulating rings. The electrodes are connected to an external resistor network, which distributes the applied high voltage across the stack and defines the axial potential gradient. This establishes the reduced reaction field strength E_{RR}/N and the reduced drift field strength E_{DR}/N. Hence, in this setup, reactant ions are selectively formed in the ion source, then transported to the reaction region where analyte ionisation occurs through the above described ion-neutral reactions. To prevent interaction of the analyte molecules with intermediates formed during reactant ion formation, the sample gas is introduced into the reaction region at the interface with the drift region and evacuated at the interface toward the ion source. This configuration prevents the neutral analytes from entering the ion source. Again, a diaphragm pump (MVP 040-2, Pfeiffer Vacuum, Germany) maintains the required pressure. The sample gas is supplied through a 1/16″ capillary (internal diameter of 250 μm), which passively meters the flow based on the pressure difference between the reaction region of the HiKE-IMS (8 mbar) and the gas mixing setup (1000 mbar). By adjusting the capillary length, the sample gas flow rate is set to 11.7 mL min^{-1}. With this arrangement, changes in E/N and water concentration within the reaction region should not affect the ion source, ensuring that a well-defined reactant ion population is maintained throughout all measurements.

All generated ions are then transported to the end of the reaction region by E_{RR}/N and subsequently introduced by the

tristate ion shutter[33] into the drift region, where the ions are analysed based on their ion mobility. Drift gas is introduced at the end of the drift region with a constant flow rate of 12 mL min^{-1} (related to a pressure of 1013.25 hPa and 293.15 K) by a mass flow controller (F-200DV-ABD, Bronkhorst Nord, Germany). It is important to consider that the drift region can also affect the ion chemistry by fragmentation of product ions or dissociation of ion-neutral clusters. In this work, a high reduced drift field strength of 120 Td is chosen, while the reduced reaction field strength is varied between 20 and 120 Td. The high E/N in the drift region can lead to significant ion heating and thus affect the observed ion populations. This effect is especially important when the E/N in the drift region exceeds the reduced reaction field strength, which is the case in most experiments of this work. This has important implications when the intermediate reaction adduct $[RI + A]^+$ is not short-lived but somewhat stable at the set E/N in the reaction region, but not in the drift region. In this case, dissociation of the adduct either to the reactant ions or to the product ions cannot be excluded, with the branching ratios given by the relative reaction rate coefficients for the individual dissociation reactions. More detailed descriptions of both instruments, as well as their most relevant operating parameters, can be found in Section S1.

Method for experimental determination of reaction rate coefficient. As outlined in the Introduction, in bimolecular reactions like proton transfer between H_3O^+ and a neutral analyte A, forming a protonated monomer AH^+ and a water molecule, the reaction rate can be described by the product of the reaction rate coefficient k_{obs} and the particle densities of both reactants, $[H_3O^+]$ and [A], as expressed in eqn (7).

$$\frac{d[AH^+]}{dt} = -\frac{d[H_3O^+]}{dt} = k_{obs}[H_3O^+][A] \quad (7)$$

Since ion densities in IMS are usually lower than those of neutral analytes,[34] the analyte concentration [A] remains relatively unchanged by the reaction, allowing the treatment of proton transfer as a pseudo-first order reaction. The ion densities of H_3O^+ after the reaction time t_R given as $[H_3O^+]_{t_R}$ can be described as an exponential decay function multiplied with its ion density before the reaction ($t_R = 0$) given as $[H_3O^+]_0$, as shown in eqn (8).

$$[H_3O^+]_{t_R} = [H_3O^+]_0 e^{-k_{obs} t_R [A]} \quad (8)$$

Charge conservation implies that the initial reactant ion density equals the sum of reactant and product ion densities after the reaction. Solving eqn (8) for the reaction rate coefficient leads to eqn (9), which demonstrates that determining reaction rate coefficients requires knowledge of reaction times and relative intensities of reactant and product ions from ion mobility spectra, alongside the known analyte vapor concentration. Since peak areas in an ion mobility spectrum correspond to the underlying charge and thus number of ions, they effectively represent relative intensities.

$$k_{obs} = -\frac{1}{[A]_{t_R}} \log\left(\frac{[H_3O^+]_{t_R}}{[H_3O^+]_{t_R} + [AH^+]_{t_R}}\right) \quad (9)$$

In the instrumental setup, reaction times are determined by the reactant ions' residence times in the reaction region, calculated as the ratio of the reaction region length to drift velocity. Field-dependent ensemble drift velocities of $H_3O^+(H_2O)_n$ and $NO^+(H_2O)_m$ are determined by recording ion mobility spectra at each E/N value from 20 and 120 Td in steps of 1 Td, extracting peak positions *via* Gaussian fitting. This provides the relationship between E/N, residence times in the reaction region, and effective temperatures. Note that such experiments only need to be conducted once for a given reactant ion species.

Next, neutral analytes are introduced to the reaction region with a constant, known vapor concentration. Ion mobility spectra are recorded at varying E/N in the reaction region from 20 and 120 Td in steps of 1 Td, influencing the ion-neutral reactions. Extracting the peak areas of reactant and product ions yields their relative intensities, which, combined with the other experimental data, allows for the calculation of reaction rate coefficients using eqn (9). It is important to note that this approach assumes a uniform distribution of neutral analytes in the reaction region, neglecting boundary effects of gas flows at the interface between ion source and reaction region. A constant analyte concentration during the residence time of reactant ions in the reaction region is a standard implicit assumption in SIFT-MS and PTR-MS kinetics,[35,36] where the neutral population is assumed to exceed the ion density and is continuously replenished by the sample gas flow. The reaction therefore proceeds under pseudo-first order conditions, and analyte depletion by reaction can be neglected to a good approximation. Additionally, it is assumed that dopant gas is only present in the ion source and sample gas solely in the reaction region. Also, the approach assumes consistent ion losses across all ion species during transport through the HiKE-IMS. This assumption is justified because all ions traverse the same reaction and drift region under identical electric fields and are injected into the drift region *via* a tristate ion shutter, which eliminates mobility-dependent discrimination as known from classical Bradbury–Nielsen gates.[33,37] Radial ion losses discussed in IMS literature occur primarily in the millisecond range,[38,39] whereas drift times in HiKE-IMS are only a few hundred microseconds. To assess whether radial diffusion could nevertheless introduce species-dependent transmission differences, we calculated transverse diffusion coefficients D_T using the generalized Nernst–Einstein relation $D_T = Kk_B T_T/q$, where T_T is the transverse ion temperature. For context, the effective ion temperature is related to the longitudinal and transverse temperatures by $T_{eff} = 1/3T_L + 2/3T_T$, *i.e.* $T_T < T_{eff}$ under our conditions.[11] For the most diffusive ions (H_3O^+ and NO^+), the resulting radial diffusion lengths remain well below 2 mm at 120 Td in the drift region (see Section S7). Given that this length remains more than an order of magnitude below the drift tube radius of 21 mm, diffusion-driven ion losses at walls and mobility-dependent transmission differences are expected to be negligible, and remaining transmission effects can be treated as approximately species-independent.

Chemicals. The chemicals benzene (CAS: 71-43-2), toluene (CAS: 108-88-3), and *p*-xylene (CAS: 95-47-6) were purchased from Sigma Aldrich Germany and used without further purification.

The sample gas is enriched with the analytes using the permeation method using a gas mixing setup explained in

detail in a previous publication.[40] Purified dry air is supplied using a zero-air generator (JAG, JAGZAG600S) and appropriate additional filters as described in earlier works.[19]

Modelling. In order to gain a deeper understanding of the found reaction rates for different reactant ions and analytes, we also conducted quantum chemical modelling of the ionisation processes using a modelling pipeline reported previously.[41] For both PT and CT, we model the first step of the ionisation process as the formation of a reaction complex composed of the charged reactant ion and neutral analyte, which can also dissociate again:

$$RI^+ + A \rightleftarrows [RI^+ + A] \quad (10)$$

In principle, within this reaction complex, charge transfer (either by proton or electron transfer) can occur

$$[RI^+ + A] \rightleftarrows [RI + A^+] \quad (11)$$

followed by dissociation of the reaction complex towards the charged analyte:

$$[RI + A^+] \rightleftarrows RI + A^+ \quad (12)$$

This formalism is slightly more general than the one outlined in the Introduction. Here, additional to the initial association rate/equilibrium and the final dissociation rate, the height (or existence) of the barrier within the reaction complex plays an important role (see Fig. 2).

Further, we consider the different hydration states and their interconversion of all ions, *i.e.*, the reactant ions, the reaction complexes, and the ionised analyte:

$$M^+(H_2O)_n + H_2O \rightleftharpoons M^+(H_2O)_{n+1} \quad (13)$$

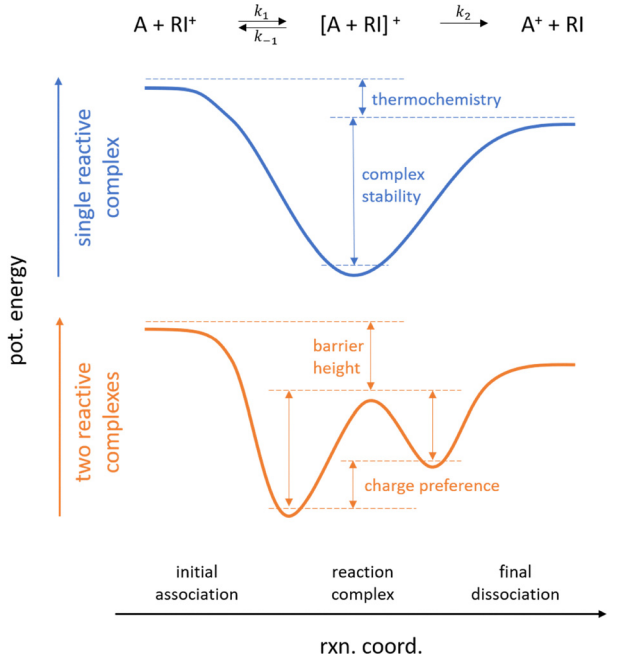

Fig. 2 Exemplary potential energy surfaces for proton and charge transfer including one (blue) or two (orange) reaction complexes.

Note that all non-covalent complexes can exist in multiple conformers, which, under thermal or activated conditions, likely interchange rapidly. See Section S3 for the full reaction schemes considered. While we cannot derive a closed form for the overall rate coefficient in this case, the limiting cases described above serve as important comparison.

To model the reaction rate coefficients for these reactions, we first used the ORCA programme package[44,45] to use density functional theory, applying the ωB97X-D3(BJ)/def2-TZVPP level of theory, to obtain the structure, thermochemistry and electrostatic properties of all species involved. For all three model analytes, we only considered one protonation site, namely the energetically most favourable one as reported in the literature for benzene,[46] toluene,[47] and *p*-xylene,[48] see Scheme 1. We also only consider one conformer per reaction complex for simplicity. Here, we pick the lowest energy conformer after exemplary sampling different complex arrangements. We further refined the electronic energies using the DLPNO-CCSD(T)/def2-TZVPP level of theory. Here, we found that the T1 diagnostic for closed-shell calculations is always below 0.0156, and for open-shell calculations, it is always below 0.0221, validating the single-reference character of our calculations. All structures (xyz files) are available in the ioChem-BD database (see Data availability statement). We then used MobCal-MPI 2.0[49] to determine the ion mobilities and effective temperatures of all species as a function of *E*/*N* in order to relate the amount of ion heating to the field strengths applied. We chose the ωB97X-D3(BJ)/def2-TZVPP level of theory as it was shown to yield the most accurate mobility and thus effective temperature results using MobCal-MPI,[50] which is important as the reaction dynamics are strongly influenced by the ion temperatures. Furthermore, the original work on the ωB97X-D3 functional benchmarked the mean absolute errors for proton affinities at 1.29 kcal mol^{-1} and for noncovalent interactions at 0.41 kcal mol^{-1}, which are sufficiently accurate for the present work.

The reactions (10)–(13) proceed either *via* loose or tight transition states (TSs). Association and dissociation reactions proceed *via* loose TSs, *i.e.*, without a barrier. These rates can be modelled using theories like the SACM theory,[51,52] where the ion-neutral interaction potential is either described by an ion–dipole or ion-induced dipole potential, depending on which is more dominant for a given neutral analyte. The rates are then computed through assuming a centrifugal barrier, which depends on

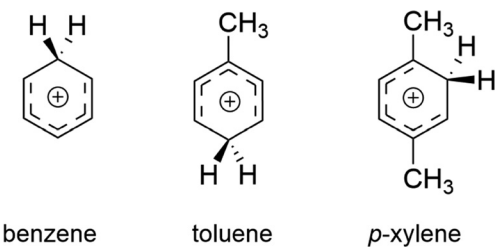

Scheme 1 Structures of the protonated analytes considered in the modelling. All analytes show a σ-bond between the proton and a carbon from the benzene ring, breaking aromaticity.

the energetics and properties of the system. Tight TSs, *i.e.*, those with a barrier, can be modelled by first optimising the structure of the stationary point and then using standard transition state theory (TST, *i.e.*, the Eyring equation[53]) to determine the rate coefficient from the molecular properties. To this end, the minimum energy reaction path between reactant and product structures was mapped using the nudged-elastic band (NEB) method[54] (climbing-image variant) as implemented in ORCA. The highest energy structure found on the reaction path is close to the true TS and was thus used as initial guess for a TS optimization (usually only a few optimization steps are needed). Structures were confirmed to only have one imaginary frequency corresponding to the reaction coordinate. The explicit expressions for the SACM and transition state theory rate coefficients are provided in Section S5. Other approaches, such as RRKM/master-equation (ME) modelling, are often regarded as the gold standard for reaction kinetics. However, for the present purpose of capturing qualitative trends, SACM offers a computationally efficient framework, as the rate coefficients can be directly derived from molecular properties without requiring explicit density-of-states calculations. Note that for the charge transfer, the potential energy surface on which the reaction occurs is diabatic because the reactants (NO^+ and B/T/X) can be well described as a singlet state, while the products ($NO^\bullet$ + $B^{\bullet+}$/$T^{\bullet+}$/$X^{\bullet+}$) each have an unpaired electron and thus are well described as a triplet state. Here, we approximate the barrier by calculating the minimum energy crossing point (MECP) of the adiabatic singlet and triplet surfaces, as was done recently elsewhere.[55]

Quantum tunnelling effects are known to play a role in PT reactions.[56] In particular, PT rates are accelerated due to quantum tunnelling when compared to treating the proton classically as done in TST. Yet, we did not include quantum tunnelling effects as these go beyond the scope of this work and only affect a small number of reactions (see below).[41]

The described formalism has been used previously to study ion-neutral reactions at elevated reduced electric field strengths and has been validated against experimental data by comparing modelled and measured reaction product distributions (*i.e.*, not directly comparing rate coefficients).[41,52,57] Here, we further implemented a pressure dependency of the computed rates *via* a simple Lindemann–Hinshelwood treatment.[58,59] To this end, the pressure-dependent rate coefficient, k_{LH}, is described as a combination of a unimolecular high-pressure rate coefficient, k_∞, and bimolecular low-pressure rate coefficient, k_0, as

$$k_{LH}^{-1} = k_\infty^{-1} + k_0^{-1} \quad (14)$$

while the high-pressure rate coefficient coincides with the TST or SACM rate coefficients, the low-pressure rate coefficient depends on the collision frequency, ν_{coll}, and the portion of the analytes that have an energy above the barrier height, $P(E > E_0)$. In the so-called strong collision limit, the low-pressure rate coefficient can be written as:[59]

$$k_0 = \nu_{coll} \cdot P(E > E_0) \quad (15)$$

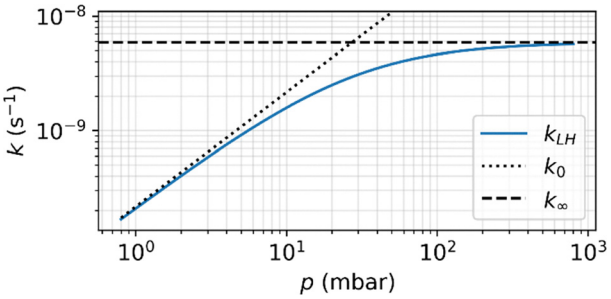

Fig. 3 Reaction rate coefficient from the Lindemann–Hinshelwood treatment k_{LH} (solid line) in comparison with the unimolecular high-pressure rate coefficient k_∞ (dashed line) and the bimolecular low-pressure rate coefficient k_0 (dotted line) for the $H_3O^+(H_2O) \rightarrow H_3O^+ + H_2O$ dissociation at 303 K, over a pressure range of 1–1000 mbar.

The collision rate depends on the reduced field strength and can be computed through the field-dependent collision cross sections, Ω, determined through MobCal-MPI 2.0 as:[11]

$$\nu_{coll} = \frac{4}{3}\sqrt{\frac{8k_B T_{eff}}{\pi\mu}}\Omega(T_{eff})N \quad (16)$$

where k_B is Boltzmann's constant, μ is the reduced mass of the ion-bath gas pair, and N is the particle density of the bath gas, which is proportional to the pressure. $P(E > E_0)$ can be computed from the internal density of states, $\rho(E)$, and the internal partition function, Q_{int}, of the analyte *via*:

$$P(E > E_0) = \frac{1}{Q_{int}}\int_{E_0}^{\infty}\rho(E)e^{-\frac{E}{k_B T_{eff}}}dE \quad (17)$$

and depends on the effective temperature as well. Fig. 3 shows the pressure dependency exemplarily for the $H_3O^+(H_2O) \rightarrow H_3O^+ + H_2O$ dissociation. Note that the actual rate coefficient is always lower than the high-pressure rate coefficient obtained *via* TST. This is in line with our previous observations, namely that we had to scale down our computed (fragmentation) rate coefficients when obtained *via* TST to match experimental data.[57]

Finally, we can model the overall ionisation yield by numerical integration of the coupled reaction rate equations corresponding to the networks outlined in the SI for the given reaction time, *i.e.*, the drift time of the reactant ions through the reaction region. More details of the used numerical integration scheme can be found in our previous publication.[41] Given the ion population distribution at the end of the reaction time, we can use eqn (9) just as in the evaluation of the experimental data.

Three-dimensional molecular structures were prepared using Avogadro.[42] All plots and kinetic data visualisations were produced in Python using Matplotlib.[43]

Results and discussion

To accurately determine the reaction rate coefficients for proton transfer of the model analytes with $H_3O^+(H_2O)_n$ and charge transfer with $NO^+(H_2O)_m$, it is essential to selectively provide these reactant ion species at high purity. The mass spectra obtained by coupling the developed ion source to the PTR-QMS

300 are shown in Section S1, demonstrating that both $H_3O^+(H_2O)_n$ and $NO^+(H_2O)_m$ can be selectively formed.[16,34]

With the confirmed selective supply of reactant ions, the reaction kinetics of proton and charge transfer of the model analytes with $H_3O^+(H_2O)_n$ and $NO^+(H_2O)_m$ can now be explored. This is achieved by coupling the developed ion source with a HiKE-IMS (see Section S1). As discussed above, we first experimentally determine the field-dependent drift velocities to calculate the reaction times and effective temperatures of the reactant ions depending on *E*/*N*. As expected, Fig. 4(a) shows that the drift velocities of the reactant ions strongly increase with *E*/*N*, exceeding the mean thermal velocity at high *E*/*N*. Consequently, the residence times of the reactant ions in the reaction region (Fig. 4(b)) substantially decrease from about 600 μs to 100 μs. This relationship between *E*/*N* and reaction time must be considered when analysing ion chemistry in HiKE-IMS.

Furthermore, increased drift velocities result in significant ion heating, raising the effective temperatures of the reactant ions well above ambient temperature to a maximum of 1400 K for H_3O^+ and 1500 K for NO^+. As discussed in the Introduction, this increased effective temperature is expected to substantially impact ion chemistry. With these correlations established, we introduce the model analytes with a constant vapor concentration of 200 ppb_v into the HiKE-IMS to further examine the reaction kinetics of proton and charge transfer with both reactant ion species. These concentrations are high enough compared to the ion densities to ensure validity of the pseudo-first order assumption, but also low enough to avoid secondary reactions with neutral analytes such as proton-bound dimer formation.

The obtained relative peak areas necessary for determination of the reaction rate coefficients are shown in Section S6. These experimental data allow for calculation of the reaction rate coefficients for the proton transfer of *p*-xylene, toluene and benzene with $H_3O^+(H_2O)_n$, and for charge transfer with $NO^+(H_2O)_m$. Leveraging the relationship between *E*/*N* and effective temperature, the observed reaction rate coefficients for proton and charge transfer are plotted against effective temperature in Fig. 6 and 8.

Proton transfer

Proton transfer from H_3O^+ to the neutral analytes is exergonic only if the neutral analyte has a higher gas-phase basicity (GB) than the water molecule. Usually, it is assumed that proton transfer occurs at each collision when the proton transfer is exothermic by more than 25 kJ mol^{-1}, ensuring $k_2 \gg k_{-1}$ (association limit).[60–62] The calculated Gibbs free energy changes (see Fig. 5) show that this should be the case if the bare H_3O^+ reacts with the three model analytes, for which the overall reaction is strongly exergonic. Moreover, we only found a single reaction complex (see Fig. S6 for structures), which is quite unstable with respect to the final products, suggesting a quick turnover and that $k_2 \gg k_{-1}$, meaning that the overall rate coefficient is well approximated by the association rate (association limit). This is confirmed by the modelled reaction rate coefficients (see Fig. S12 for a detailed comparison). When the

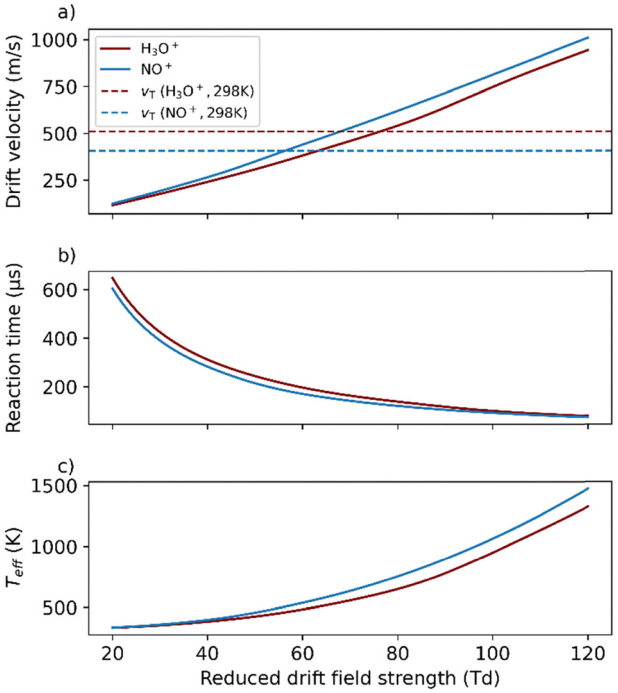

Fig. 4 Experimental data of the reactant ions $H_3O^+(H_2O)_n$ and $NO^+(H_2O)_n$ used for calculation of the reaction rate coefficients. (a) Drift velocities compared to thermal velocities v_T at 298 K and calculated (b) reaction times and (c) effective temperatures. The ion source parameters are detailed in Section S1. All other operating parameters according to Table S2.

hydrates of H_3O^+ are involved, we find that ionisation proceeds *via* a ligand switching mechanism (*cf.* Fig. 2 (orange PES) and Fig. S6 for structures) where a water molecule is replaced by the neutral analyte. In ionisation involving hydrates of H_3O^+, the Gibbs energy change of the reaction depends both on the GB and the Gibbs energy changes associated with hydration of both H_3O^+ and the protonated analyte.[19] In these cases, not only high GB, but also energetically favourable hydration of the protonated monomer improves ionisation efficiency. Hydration of H_3O^+ can make ionisation more endergonic compared to ionisation *via* bare H_3O^+, potentially reducing ionisation efficiency. This often results in lower sensitivity in IMS at high water concentrations where the reactant ions form hydrates with often several water molecules.[63,64]

Due to their low GB, the investigated aromatic hydrocarbons are not efficiently ionised by larger hydrates of H_3O^+ present at low *E*/*N* or low effective temperatures. Previous studies on their ion chemistry in HiKE-IMS suggest that *p*-xylene and toluene react with the monohydrate of H_3O^+, present above 500 K, while benzene requires bare H_3O^+, present above 800 K, as it has the lowest GB of the three model analytes.[17,19] With larger hydrates of H_3O^+, reactions are endergonic, as shown from the Gibbs free energy levels in Fig. 5. Moreover, the reaction complex where the analyte only acts as a neutral ligand, *i.e.*, $[RI^+ + A]$ is quite stable compared to the dissociated reaction products, rendering it a thermodynamic sink. This is amplified by the fact that the expected multi-conformer nature of the reaction complex lowers its Gibbs free energy level due to an increase in

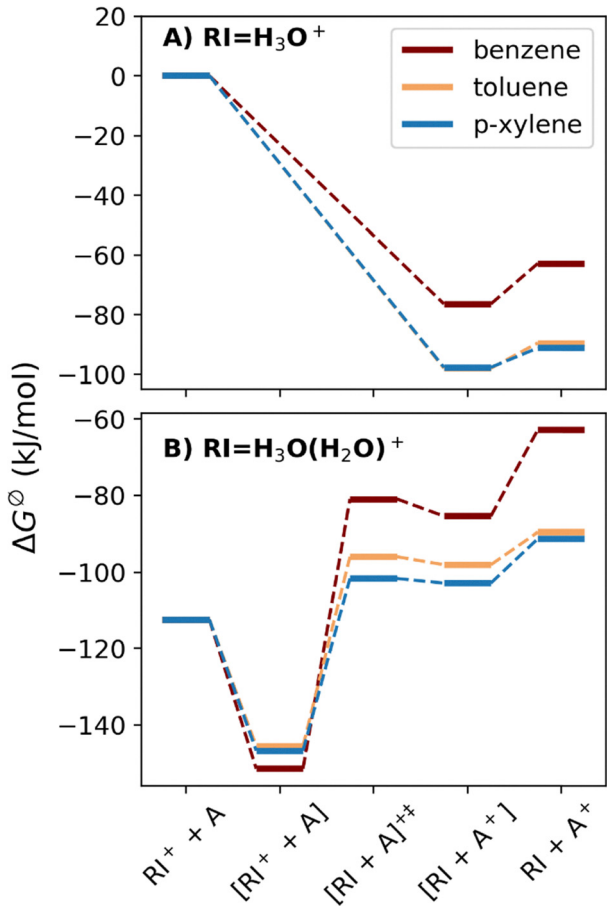

Fig. 5 Computed Gibbs energy levels for the reactants, products, and intermediate reaction complexes of proton transfer from (A) H_3O^+ and (B) $H_3O^+(H_2O)$ with benzene, toluene, and *p*-xylene. Computed zero-point energy levels can be found in Fig. S10.

entropy. This means that the reaction complex is not short-lived and the limiting case (association limit) does not apply here. Indeed, our modelling shows that the forward rate coefficient k_2 is well below the reverse rate coefficient k_{-1} (Fig. S13) which would correspond to the limiting case (limit 1) defined in the Introduction, *i.e.*, only the small portion of the reaction complex formed in equilibrium (k_1[A]/k_{-1}) may react to the products. The small values of k_2 are partially resulting from it describing a tight transition state with low entropy (conformational change) as opposed to the loose transition state observed for dissociation reactions. Moreover, the second reaction complex structure [RI + A^+] again has two reaction channels, namely back to the initial complex [RI^+ + A] or forward to the products, further slowing down the overall reaction turnover. Note that quantum tunnelling effects could accelerate the transition over the barrier connecting [RI^+ + A] and [RI + A^+] within the reaction complex, leading to a quicker equilibration between them. Yet, as the threshold of the dissociated products is well above the internal PT barrier, this should not significantly alter the overall rate. In total, the reaction complexes for this system are stable enough that they are predominantly formed under comparably low field conditions (see Fig. S13). This means that the observed reaction rate coefficient will be below the limit 2 rate (association limit) when hydrates of H_3O^+ dominate the reactant ion population (Fig. S15).

The computed Gibbs free energy levels suggest that this effect should be more severe for benzene than for toluene and *p*-xylene: while the reaction complexes [$H_3O^+(H_2O)$ + A] show similar stability for all model analytes (similar charge–π interaction, *cf.* Fig. S6), the increasing GB from benzene to *p*-xylene renders the proton transfer from $H_3O^+(H_2O)$ less endergonic. In other words, a stronger GB of the analyte leads to less stable reaction complexes with respect to dissociation towards the reaction products, ensuring more efficient reaction turnover. These data further suggest that even higher hydrates of H_3O^+, namely $H_3O^+(H_2O)_2$ and larger cannot protonated the chosen model analytes efficiently, which is why their reactions were not considered here.

From the used numerical integration scheme,[41] we obtain the ion population distribution at the end of the reaction region for each *E*/*N*, consisting of H_3O^+ and its hydrates as well as the product ions (see Fig. S13).

At low effective temperature, the hydration of H_3O^+ leads to the observed reaction rate coefficients being substantially lower than the association rate (k_{lim2}) as shown in Fig. 6(a). For toluene and *p*-xylene, although proton transfer even with $H_3O^+(H_2O)$ is possible, the internal barrier between the reaction complexes, despite its small height (see Fig. 5), slows down the overall conversion rate.

For benzene, in particular, the reaction rate coefficient drops between 400 K and 600 K, because the simple formal kinetic description is not valid anymore. In particular, larger adducts (such as [B + H + $2H_2O$]$^+$) are mostly formed in the reaction

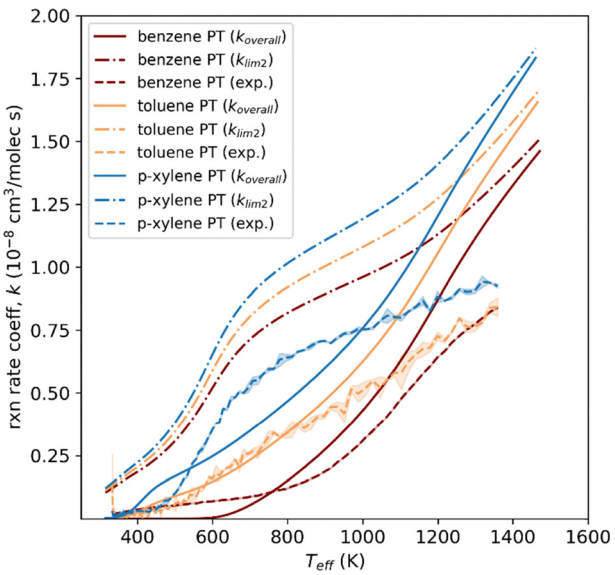

Fig. 6 Modelled and experimentally observed (dashed line) reaction rate coefficients for the proton transfer from $H_3O^+(H_2O)_n$ to *p*-xylene, toluene, and benzene depending on effective temperature, including both the modelled overall reaction rate coefficient (solid line) and the reaction rate coefficient k_{lim2} when assuming association limit (dash-dot line). The analyte concentration was set to 200 ppb_V. The ion source parameters are detailed in Section S1. All other operating parameters according to Table S2.

region that are quite stable (see Fig. S13). These can form *via* B + $H_3O^+(H_2O)$ but also *via* association of $[B + H + H_2O]^+$ with water molecules. Since $[B + H + 2H_2O]^+$ can also dissociate back to the reactants ($B + H_3O^+(H_2O)$) quite easily, the overall conversion rate is slowed down.

Hence, the deviation between k_{lim2} and the observed reaction rate coefficients can be attributed to significant contribution of ionisation through larger hydrates of H_3O^+ with more complicated reaction mechanisms (*e.g.* from additional adducts) and the ignored interconversion (see above).

This is in line with the experimentally observed reaction rate coefficients in Fig. 6(b), where a strong increase in the reaction rate coefficients with increasing effective temperature can be seen. This can again be associated with the thermodynamics affecting the reaction turnover under certain conditions (here, particularly at low *E*/*N*). Earlier studies on the reactant ion populations in HiKE-IMS have shown that $H_3O^+(H_2O)$ and H_3O^+ can be observed above effective temperatures of 500 K and 800 K, respectively.[19] However, since the earlier work included a coupling to a mass spectrometer, additional dissociation of the hydrates within the transfer stages cannot be excluded. Nevertheless, the observed reaction rate coefficients depending on effective temperature are in good agreement with expectations: as $H_3O^+(H_2O)_n$ forms the monohydrate at 500 K, the observed reaction rate coefficients for *p*-xylene and toluene increase, and similarly for benzene when the bare H_3O^+ forms at 800 K. Since average cluster sizes decrease with increasing *E*/*N* and effective temperature, a greater fraction of reactant ions can ionise the analytes *via* proton transfer, resulting in an increase in observed reaction rate coefficients even up to the maximum effective temperature of 1400 K.

Given the high stability of the reaction complex for larger hydrates of H_3O^+ and the lack of any reaction complexes in the experimental data, we turned to an investigation of the influence of the drift region. Here, a reduced drift field strength of 120 Td is applied, resulting in high ion activation and rendering most adducts unstable. Indeed, our modelling results show that the reaction complexes formed in the reaction region under low reduced field strengths quickly dissociate in the drift region (see Fig. S14). Importantly, this occurs with a branching ratio determined by the rate coefficients k_2 and k_{-1} evaluated at 120 Td. This means that more reaction complexes are formed in the reaction region than reaction products are finally observed at the end of the drift region.

To estimate the error this introduces in our formalism of experimentally determining the total reaction rate coefficients, we computed the rate coefficients considering the ion populations at the end of the reaction region (*i.e.*, the true reaction rate coefficient (see Fig. S15) and considering the ion populations at the end of the drift region (observed reaction rate coefficient). As can be seen in Fig. S15, there is a deviation between the reaction rate coefficients for these two cases. However, a substantial difference can only be observed for benzene (lowest GB) and only at low *E*/*N*. In this range, in particular, the reaction rate coefficients are very small anyways (see also the large standard deviation in the experiment under such conditions), meaning that the error introduced by the drift region setup is negligible.

While the agreement is only qualitative, the modelled rate coefficients reproduce the order of magnitude, the ordering (with respect to the analytes) and certain shape aspects of the experimental rate coefficients. At low effective temperatures, the absolute reaction rate coefficients are very small, leading to correspondingly weak ion signals and, consequently, large relative experimental uncertainties. On a logarithmic scale, these relative fluctuations appear amplified, giving rise to noticeable deviations from the theoretical prediction, despite the small absolute differences. At intermediate T_{eff}, systematic offsets can arise from subtle differences in hydration equilibria or intermediate stabilisation, for example, in the case of *p*-xylene, where slightly reduced clustering in the experiment may yield higher apparent reaction rate coefficients than predicted. In this context, the absolute water concentration in the reaction region cannot be determined with high accuracy at the operating pressure of 8 mbar, as small contributions from permeation through seals, back-diffusion, or dilution effects may slightly shift the effective hydration environment. At high effective temperatures, where hydration is largely suppressed, and reactions approach the association rate (association limit), the experimental and theoretical curves exhibit the same asymptotic trend.

Hence, the results on proton transfer with $H_3O^+(H_2O)_n$ show that reaction thermodynamics significantly influence the experimentally observed reaction rate coefficients, especially the stability of reaction complexes and overall Gibbs free energy change. The difference in observed reaction rate coefficients among the three model analytes can therefore be attributed in part to the differences in their GB as well as the different stabilities of the reaction complex compared to the final products.

Charge transfer

The charge transfer from NO^+ to the neutral analytes is exothermic if the ionisation energy (IE) of the neutral is below that of NO. Again, hydration of the reactant ion, which can occur especially at low *E*/*N*, leads to a more endergonic reaction, potentially reducing ionisation efficiency of analytes with an IE close to NO. Fig. 7 shows the Gibbs free energy levels of the reaction steps involved for no hydration and with a single water adducts. Generally, we find that hydration of the charge transfer reaction complexes does not release significant energy as their zero-point energy levels and Gibbs free energy levels are only slightly below the levels of the bare reaction complexes. This means that the pathway *via* hydrated NO^+ only plays a minor role, and we will focus on the bare ion charge transfer path.

Here, the reaction complex is quite stable in the singlet configuration ($^1[NO^+ + A]$) but the corresponding triplet minimum ($^3[NO^\bullet + A^{+\bullet}]$) is very shallow. Again, it can be expected that the Gibbs free energy levels of the reaction complexes are slightly lowered by an increased entropy due to the expected multiconformer nature of these loosely bound species. Given this fact and the structure of the two crossing surfaces (including the intersystem crossing pathway), we will ignore the triplet state for the following discussion and assume that the singlet state can directly dissociate towards the reaction products (as well as back to the reactants). See Section S3 for further discussion.

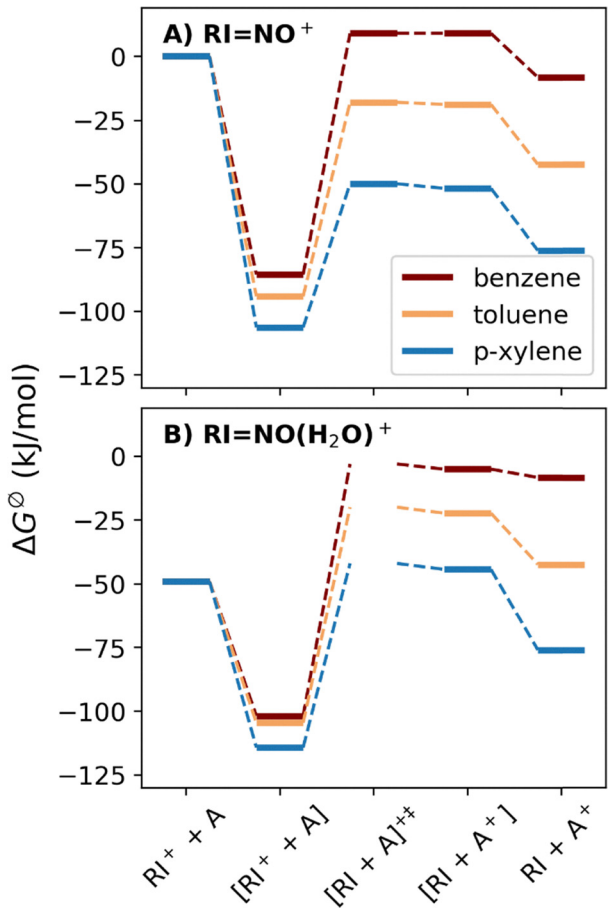

Fig. 7 Computed Gibbs free energy levels for the reactants, products, and intermediate reaction complexes of proton transfer from (A) NO^+ and (B) $NO^+(H_2O)$ with benzene, toluene, and *p*-xylene. Transition states in (A) correspond to the MECP of the singlet and triplet surface. Note that the final products, RI + A^+, appear below the reaction complexes only due to the entropy contribution in the Gibbs free energies. Computed zero-point energy levels can be found in Fig. S11 and show an energy increase from the reaction complexes towards the products. This also means that quantum tunnelling could (if at all) only occur through the internal CT barrier between the reaction complexes ($[RI + A]^{+‡}$).

We applied the same modelling approach for the reaction rate coefficients of the charge transfer as we did for the proton transfer. The complete reaction scheme considered is given in Fig. S4. As discussed above, a stable reaction complex can lead to a reduced ionisation rate when compared to the association limit. For the three model analytes considered here, the stability of the reaction complexes with respect to the reactants is very similar (corresponding to a ZPE level difference of about 1.5 eV, see Fig. S11), which is reasonable given that in all three cases the charge located at the NO is stabilised *via* similar π–π-interactions (see Fig. S7 for structures). However, the stability of the reaction complexes with respect to the final products varies greatly (*cf.* Fig. 7) because of the different IE of the three analytes. In particular, the reaction complex for benzene is very stable, whereas the reaction complex of *p*-xylene is much weaker. Therefore, for benzene, k_2 is very similar to k_{-1} over the whole range studied, whereas for toluene and *p*-xylene, k_2 is always greater than k_{-1}, meaning more favourable ionisation (see Fig. S16). It should be noted that in Fig. 7, the dissociated products, RI + A^+, appear below the reaction complexes only in terms of Gibbs free energy, owing to entropic contributions. The corresponding ZPE levels (Fig. S11) instead show an increase in energy from the reaction complexes towards the products. As a result, quantum tunnelling may only affect charge transfer across the internal CT barrier separating the two reaction complexes ($[RI^+ + A] \rightleftarrows [RI + A^+]$) but does not provide a tunnelling pathway towards product formation.

At low *E*/*N*, the reaction complex will dissociate only slowly, even for toluene and *p*-xylene and as such accumulate in the reaction region. Only in the high *E*/*N* of 120 Td of the drift region, these reaction complexes then dissociate quickly according to the branching ratio k_2/k_{-1} at 120 Td. As we find this ratio to be quite favourable for the product formation (*cf.* Fig. S16), we finally find very little deviation between the observed rate coefficients and the association limit, see Fig. 8(a). Only benzene shows a lower reaction rate coefficient due to the very small difference in IE between benzene and NO. The high stability of its reaction complex is also reflected in its experimental observation in previous studies.[65] In terms of the influence of the drift region, we again find that it only introduces a small error to the experimental determination of reaction rate coefficients and only if the difference in IE between reactant ion and analyte is small (see Fig. S17).

Despite this, the modelling results highlight that the association between A and NO^+ is the limiting step for reaction kinetics if there is a significant difference in IE, which is why the association rate coefficient is in good agreement with the observed reaction rate coefficient for toluene and *p*-xylene. A similar finding has

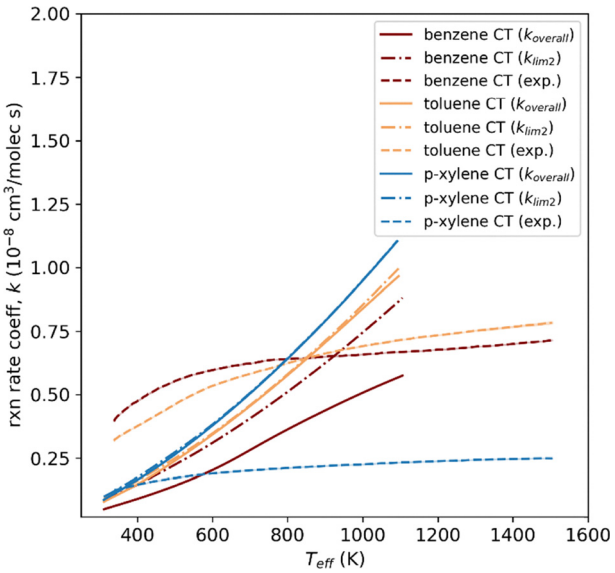

Fig. 8 Modelled and experimentally observed (dashed line) reaction rate coefficients for the charge transfer from $NO^+(H_2O)_m$ to *p*-xylene, toluene, and benzene depending on effective temperature, including both the modelled overall reaction rate coefficient (solid line) and the reaction rate coefficient k_{lim2} when assuming association limit (dash-dot line). The analyte concentration was set to 200 ppb_V. The ion source parameters are detailed in Section S1. All other operating parameters according to Table S2.

already been obtained for the proton transfer from H_3O^+ to the analytes, provided that the reaction is thermodynamically allowed, which agrees well with typical findings from the literature showing that proton and charge transfer can often occur at each collision.[6,61,62]

Comparing the computed and experimentally observed reaction rate coefficients (Fig. 8) yields a good qualitative agreement. In particular, the order of magnitude is well matched and similar to the proton transfer, an asymptotic behaviour towards high E/N can be found, as the observed reaction rate coefficient approaches the association rate. The comparison also suggests that the modelling overestimates the increase in the association rate with reduced field strength, as the asymptotic behaviour is more pronounced in the experimental data. This has similarly been observed for the proton transfer data. In contrast to proton transfer, no indication of significant hindrance of the charge transfer resulting from hydration at low E/N can be observed. Since the dissociation of NO^+ hydrates requires a lower effective temperature due to the lower hydration enthalpy of NO^+ (77.4 kJ mol^{-1})[21] compared to H_3O^+ (133 kJ mol^{-1}),[66] previous work has shown that the bare NO^+ is present above 600 K. The modelling predicts that analytes with larger difference in IE between the reactant and analyte should exhibit higher reaction rate coefficients and approach the association rate more closely. This trend is not reproduced experimentally: *p*-xylene, for which the model predicts the highest rate coefficient due to its IE, consistently shows the lowest experimental rate coefficients. As the absolute NO^+ rate coefficients remain relatively large (compared to H_3O^+ reactions) at low T_{eff}, this deviation cannot be explained by signal-to-noise limitations. Moreover, as hydration plays only a minor role for NO^+, differences in clustering dynamics are unlikely to account for this deviation. Instead, the data indicate a systematic offset for *p*-xylene that is conserved over the full T_{eff} range, while the overall functional dependence on T_{eff} is well reproduced. This suggests that small analyte-specific differences, *e.g.* in the experimental transfer efficiencies—which are not represented in the simplified model—may shift the absolute rate coefficients without altering their dependence on T_{eff}. At high T_{eff}, where clustering is fully suppressed and the reaction proceeds in the transition towards the collision-controlled regime, the experimental trends for all three analytes converge towards the same qualitative asymptotic behaviour predicted by the model. However, *p*-xylene retains the same constant offset relative to benzene and toluene even in this regime, indicating that the discrepancy is not linked to a specific T_{eff} range but rather reflects a small, analyte-dependent systematic shift that is beyond the resolution of the current model. On the other hand, the differences between the experimentally observed reaction rate coefficients are quite small (given the range of rate coefficients that we find in the modelling). Therefore, this could point towards the overall accuracy of the experimental method.

Conclusions

This work provides an in-depth investigation of the field-dependent reaction kinetics on proton transfer from $H_3O^+(H_2O)_n$ and charge transfer from $NO^+(H_2O)_m$ to the aromatic hydrocarbons benzene, toluene and *p*-xylene based on experimental studies using HiKE-IMS combined with quantum chemical modelling of the ionisation processes. The results show that ionisation rates can approach the association rates, *i.e.*, every formation of a reaction complex leads to ionisation of the neutral analyte, for example when ionisation occurs *via* bare H_3O^+ and NO^+ and given an exothermic reaction. The association rates themselves are determined by the ion-neutral interaction potential and are analyte-specific. More complex behaviour and thus a reduced ionisation rate can be observed when the reactant ions form hydrates, as internal barriers can slow down the reaction or the reaction even becomes endergonic. In case of similar ionisation energies or proton affinities between the neutral precursor of the reactant ion and the neutral analyte, the intermediate reaction complex might dissociate back to the reactant ions or towards the products with significant contributions of both dissociation channels, which can further slow down the ionisation rate as compared to the association rate. Here, the stability of the reaction complex as determined by the specific type of binding, plays an important role.

Generally, we find that an increase of E/N (and thus an increase in the effective temperature) leads to a higher ionisation rate (and thus efficiency), as (A) the reactant ions become less hydrated and thus thermodynamically less stable, (B) the reaction complexes dissociate more quickly and thus ensure a higher turnover rate, and (C) the initial association rate increases due to the ion-neutral collision dynamics. Thus, in general, for a constant reaction time, the reaction at higher E/N would yield a higher ionisation yield. Note that in the HiKE-IMS used in this work, however, the reaction time decreases at higher E/N, so the ionization yield can decrease in this case. The possibility that stable reaction complexes are formed should always be kept in mind.

The quantitative field-dependent rate coefficients obtained in this study offer direct guidance for optimising ionization conditions in PTR-MS, SIFT-MS, and HiKE-IMS instruments. In particular, the data identify the E/N values at which ionization proceeds at the collision limit, as the bare H_3O^+ and NO^+ dominate, thereby maximising ionization efficiency. The results also show where hydration or complex stability can slow down reaction turnover, highlighting operating conditions where sensitivity loss is expected. Combined with computational insight into intermediate stability and reaction barriers, this information can be used to further optimize ion sources and drift regions that minimize undesired cluster formation or promote the rapid dissociation of intermediates, thereby improving overall signal intensities and analytical performance.

These findings are not only limited to the reactant ions used in this work but should also apply to NH_4^+ and $O_2^{+\bullet}$ ionising neutral analytes *via* proton transfer and charge transfer, respectively. Note that the model analytes investigated in this work were chosen as these exhibit no significant reaction products other than the protonated monomer and the radical cation and thus particularly no fragments. For other analytes, particularly when using $O_2^{+\bullet}$ as reactant ion, the fragmentation of product ions can further complicate the product ion formation and introduce an additional product branching.

These results also highlight that the presented instrumental modification to HiKE-IMS renders it a valuable tool for the investigation of reaction dynamics of bimolecular reactions at high effective temperatures, potentially providing more insights into such bimolecular reactions in subsequent studies. Further, the direct comparison of modelled and measured reaction rate coefficients showing satisfactory agreement provides high confidence to use the presented modelling approach in future work.

Author contributions

Christoph Schaefer: writing – original draft, conceptualization, data curation, methodology, software, visualization, validation; Alexander Haack: writing – original draft, data curation, conceptualization, methodology, software, visualization, validation; Charlotte Hellwig: writing – review & editing, formal analysis, investigation, data curation; Jannik Wuttke: writing – review & editing, investigation, formal analysis, data curation; Stefan Zimmermann: writing – review & editing, project administration, resources, funding acquisition, supervision.

Conflicts of interest

There are no conflicts to declare.

Data availability

Supplementary information: these contain more detailed descriptions of the instrumental setup, the formal kinetic treatment of proton and charge transfer, reaction schemes, modelled ion structures, and detailed information on the modelling of reaction rate coefficients as well as experimentally obtained peak areas (PDF). Additionally, the SI contains the modelled and experimentally obtained rate coefficients (XLSX) as well as data on T1 diagnostics for the performed CCSD(T) calculations (XLSX). See DOI: https://doi.org/10.1039/d5cp03612g.

All chemical structures (xyz coordinates and energies) can be found on the ioChem-BD database. The water clusters, already calculated in a previous study,[41] are available in the ioChem-BD repository[67] and can be accessed *via* https://doi.org/10.19061/iochem-bd-6-200, while the remaining structures can be accessed *via* https://doi.org/10.19061/iochem-bd-6-570.

Acknowledgements

Funded by the Deutsche Forschungsgemeinschaft (DFG, German Research Foundation) – 390583968. The authors would like to acknowledge the LUH Compute Cluster located at and funded by the Leibniz University Hannover, Germany, on which the computations of this work were conducted. The authors thankfully acknowledge the storage resources at BSC provided to ioChem-BD. We gratefully acknowledge the Bundeswehr Research Institute for Protective Technologies and CBRN Protection (WIS) for kindly providing access to the PTR-QMS 300 instrument, which was used for identification of reactant ions.

References

1 R. S. Blake, P. S. Monks and A. M. Ellis, Proton-transfer reaction mass spectrometry, *Chem. Rev.*, 2009, **109**, 861–896.
2 W. Lindinger, A. Hansel and A. Jordan, Proton-transfer-reaction mass spectrometry (PTR-MS): on-line monitoring of volatile organic compounds at pptv levels, *Chem. Soc. Rev.*, 1998, **27**, 347–354.
3 D. Smith, P. Španěl, N. Demarais, V. S. Langford and M. J. McEwan, Recent developments and applications of selected ion flow tube mass spectrometry (SIFT-MS), *Mass Spectrom. Rev.*, 2023, e21835.
4 M. Müller, F. Piel, R. Gutmann, P. Sulzer, E. Hartungen and A. Wisthaler, A novel method for producing NH4+ reagent ions in the hollow cathode glow discharge ion source of PTR-MS instruments, *Int. J. Mass Spectrom.*, 2020, **447**, 116254.
5 A. Jordan, S. Haidacher, G. Hanel, E. Hartungen, J. Herbig, L. Märk, R. Schottkowsky, H. Seehauser, P. Sulzer and T. D. Märk, An online ultra-high sensitivity Proton-transfer-reaction mass-spectrometer combined with switchable reagent ion capability (PTR + SRI-MS), *Int. J. Mass Spectrom.*, 2009, **286**, 32–38.
6 D. Smith, M. J. McEwan and P. Španěl, Understanding Gas Phase Ion Chemistry Is the Key to Reliable Selected Ion Flow Tube-Mass Spectrometry Analyses, *Anal. Chem.*, 2020, **92**, 12750–12762.
7 G. H. Wannier, Motion of Gaseous Ions in Strong Electric Fields, *Bell Syst. Tech. J.*, 1953, **32**, 170–254.
8 J. De Gouw, C. Warneke, T. Karl, G. Eerdekens, C. Van Der Veen and R. Fall, Sensitivity and specificity of atmospheric trace gas detection by proton-transfer-reaction mass spectrometry, *Int. J. Mass Spectrom.*, 2003, **223**, 365–382.
9 M. Allers, A. T. Kirk, M. Eckermann, C. Schaefer, D. Erdogdu, W. Wissdorf, T. Benter and S. Zimmermann, Positive Reactant Ion Formation in High Kinetic Energy Ion Mobility Spectrometry (HiKE-IMS), *J. Am. Soc. Mass Spectrom.*, 2020, **31**, 1291–1301.
10 E. V. Krylov and E. G. Nazarov, Electric field dependence of the ion mobility, *Int. J. Mass Spectrom.*, 2009, **285**, 149–156.
11 E. A. Mason and E. W. McDaniel, *Transport Properties of Ions in Gases*, Wiley, 1988.
12 P. Brown, P. Watts, T. D. Märk and C. A. Mayhew, Proton transfer reaction mass spectrometry investigations on the effects of reduced electric field and reagent ion internal energy on product ion branching ratios for a series of saturated alcohols, *Int. J. Mass Spectrom.*, 2010, **294**, 103–111.
13 P. E. Fowler, J. Z. Pilgrim, G. Lee and G. A. Eiceman, Field induced fragmentation spectra from reactive stage-tandem differential mobility spectrometry, *Analyst*, 2020, **145**, 5314–5324.
14 A. Bohnhorst, A. T. Kirk, Y. Yin and S. Zimmermann, Ion Fragmentation and Filtering by Alpha Function in Ion Mobility Spectrometry for Improved Compound Differentiation, *Anal. Chem.*, 2019, **91**, 8941–8947.
15 J. Langejuergen, M. Allers, J. Oermann, A. Kirk and S. Zimmermann, High kinetic energy ion mobility spectrometer: Quantitative analysis of gas mixtures with ion mobility spectrometry, *Anal. Chem.*, 2014, **86**, 7023–7032.

16 M. Allers, A. T. Kirk, C. Schaefer, D. Erdogdu, W. Wissdorf, T. Benter and S. Zimmermann, Field-Dependent Reduced Ion Mobilities of Positive and Negative Ions in Air and Nitrogen in High Kinetic Energy Ion Mobility Spectrometry (HiKE-IMS), *J. Am. Soc. Mass Spectrom.*, 2020, **31**, 2191–2201.
17 M. Allers, A. T. Kirk, C. Schaefer, F. Schlottmann and S. Zimmermann, Formation of positive product ions from substances with low proton affinity in high kinetic energy ion mobility spectrometry, *Rapid Commun. Mass Spectrom.*, 2021, **35**, e8998.
18 C. Schaefer, F. Schlottmann, A. T. Kirk and S. Zimmermann, Influence of Sample Gas Humidity on Product Ion Formation in High Kinetic Energy Ion Mobility Spectrometry (HiKE-IMS), *J. Am. Soc. Mass Spectrom.*, 2022, **33**, 1048–1060.
19 C. Schaefer, M. Allers, A. T. Kirk, F. Schlottmann and S. Zimmermann, Influence of Reduced Field Strength on Product Ion Formation in High Kinetic Energy Ion Mobility Spectrometry (HiKE-IMS), *J. Am. Soc. Mass Spectrom.*, 2021, **32**, 1810–1820.
20 F. Weiss, C. Schaefer, V. Ruzsanyi, T. Märk, G. Eiceman, C. A. Mayhew and S. Zimmermann, High Kinetic Energy Ion Mobility Spectrometry – Mass Spectrometry investigations of four inhalation anaesthetics: isoflurane, enflurane, sevoflurane and desflurane, *Int. J. Mass Spectrom.*, 2022, **475**, 116831.
21 M. A. French, L. P. Hills and P. Kebarle, Kinetics and Temperature Dependence of the Hydration of NO+ in the Gas Phase, *Can. J. Chem.*, 1973, **51**, 456–461.
22 L. Angel and A. J. Stace, The critical hydration reactions of NO+ and NO2+, *J. Chem. Phys.*, 1998, **109**, 1713–1715.
23 A. Good, D. A. Durden and P. Kebarle, Mechanism and Rate Constants of Ion–Molecule Reactions Leading to Formation of H + (H2O)n in Moist Oxygen and Air, *J. Chem. Phys.*, 1970, **52**, 222–229.
24 M. Pavlik and J. D. Skalny, Generation of [H3O] + (H2O)(n) clusters by positive corona discharge in air, *Rapid Commun. Mass Spectrom.*, 1997, **11**, 1757–1766.
25 F. C. Fehsenfeld and E. E. Ferguson, Origin of water cluster in the D region, *J. Geophys. Res.*, 1969, **74**, 2217–2222.
26 C. J. Howard, V. M. Bierbaum, H. W. Rundle and F. Kaufman, Kinetics and mechanism of the formation of water cluster ions from O2+ and H2O, *J. Chem. Phys.*, 1972, **57**, 3491–3497.
27 A. Bohnhorst, A. T. Kirk and S. Zimmermann, Simulation aided design of a low cost ion mobility spectrometer based on printed circuit boards, *Int. J. Ion Mobility Spectrom.*, 2016, **19**, 167–174.
28 F. Schlottmann, A. T. Kirk, M. Allers, A. Bohnhorst and S. Zimmermann, High Kinetic Energy Ion Mobility Spectrometry (HiKE-IMS) at 40 mbar, *J. Am. Soc. Mass Spectrom.*, 2020, **31**, 1536–1543.
29 P. Španěl, A. Spesyvyi and D. Smith, Electrostatic Switching and Selection of H3O+, NO+, and O2+ Reagent Ions for Selected Ion Flow-Drift Tube Mass Spectrometric Analyses of Air and Breath, *Anal. Chem.*, 2019, **91**, 5380–5388.
30 M. Malásková, D. Olivenza-León, F. Piel, P. Mochalski, P. Sulzer, S. Jürschik, C. A. Mayhew and T. D. Märk, Compendium of the reactions of H3O+ with selected ketones of relevance to breath analysis using proton transfer reaction mass spectrometry, *Front. Chem.*, 2019, **7**, 401.
31 A. Spesyvyi, D. Smith and P. Španěl, Selected Ion Flow-Drift Tube Mass Spectrometry: Quantification of Volatile Compounds in Air and Breath, *Anal. Chem.*, 2015, **87**, 12151–12160.
32 C. Schaefer, M. Lippmann, M. Beukers, N. Beijer, B. van de Kamp, J. Knotter and S. Zimmermann, Detection of Triacetone Triperoxide by High Kinetic Energy Ion Mobility Spectrometry, *Anal. Chem.*, 2023, **95**, 17099–17107.
33 A. T. Kirk, D. Grube, T. Kobelt, C. Wendt and S. Zimmermann, High-Resolution High Kinetic Energy Ion Mobility Spectrometer Based on a Low-Discrimination Tristate Ion Shutter, *Anal. Chem.*, 2018, **90**, 5603–5611.
34 G. A. Eiceman, Z. Karpas and H. H. Hill, *Ion mobility spectrometry*, CRC Press Inc, Boca Raton, 3rd edn, 2013.
35 D. Smith and P. Španěl, Selected ion flow tube mass spectrometry (SIFT-MS) for on-line trace gas analysis, *Mass Spectrom. Rev.*, 2005, **24**, 661–700.
36 J. de Gouw and C. Warneke, Measurements of volatile organic compounds in the earth's atmosphere using proton-transfer-reaction mass spectrometry, *Mass Spectrom. Rev.*, 2007, **26**, 223–257.
37 I. Wolańska, K. Piwowarski and J. Puton, Conservation of the Charge in Signal from Drift Tube Ion Mobility Spectrometers, *Anal. Chem.*, 2024, **96**, 17337–17344.
38 G. A. Eiceman, E. G. Nazarov, J. E. Rodriguez and J. A. Stone, Analysis of a drift tube at ambient pressure: Models and precise measurements in ion mobility spectrometry, *Rev. Sci. Int.*, 2001, **72**, 3610–3621.
39 H. R. Shamlouei and M. Tabrizchi, Transmission of different ions through a drift tube, *Int. J. Mass Spectrom.*, 2008, **273**, 78–83.
40 C. Schaefer, M. Lippmann, C. Schindler, M. Beukers, N. Beijer, M. Hitzemann, B. van de Kamp, R. Peters, J. Knotter and S. Zimmermann, Pursuing drug laboratories: Analysis of drug precursors with High Kinetic Energy Ion Mobility Spectrometry, *Forensic Sci. Int.*, 2024, **363**, 112196.
41 A. Haack, C. Schaefer, S. Zimmermann and W. S. Hopkins, Validation of Field-Dependent Ion-Solvent Cluster Modeling via Direct Measurement of Cluster Size Distributions, *J. Am. Soc. Mass Spectrom.*, 2023, **34**, 1035–1046.
42 M. D. Hanwell, D. E. Curtis, D. C. Lonie, T. Vandermeersch, E. Zurek and G. R. Hutchison, Avogadro: an advanced semantic chemical editor, visualization, and analysis platform, *J. Cheminf.*, 2012, **4**, 17.
43 J. D. Hunter, Matplotlib: A 2D Graphics Environment, *Comput. Sci. Eng.*, 2007, **9**, 90–95.
44 F. Neese, The ORCA program system, *Wiley Interdiscip. Rev.: Comput. Mol. Sci.*, 2012, **2**, 73–78.
45 F. Neese, Software update: The ORCA program system—Version 5.0, *Wiley Interdiscip. Rev.: Comput. Mol. Sci.*, 2022, **12**, e1606.
46 N. Solcà and O. Dopfer, Protonated Benzene: IR Spectrum and Structure of C6H7, *Angew. Chem., Int. Ed.*, 2002, **41**, 3628–3631.
47 D. Schröder, H. Schwarz, P. Milko and J. Roithová, Dissociation Routes of Protonated Toluene Probed by Infrared Spectroscopy in the Gas Phase, *J. Phys. Chem. A*, 2006, **110**, 8346–8353.

48 B. Arstad, S. Kolboe and O. Swang, Theoretical study of protonated xylenes: ethene elimination and H,C-scrambling reactions, *J. Phys. Org. Chem.*, 2004, **17**, 1023–1032.
49 A. Haack, C. Ieritano and W. S. Hopkins, MobCal-MPI 2.0: an accurate and parallelized package for calculating field-dependent collision cross sections and ion mobilities, *Analyst*, 2023, **148**, 3257–3273.
50 C. Ieritano and W. S. Hopkins, Assessing collision cross section calculations using MobCal-MPI with a variety of commonly used computational methods, *Mater. Today Commun.*, 2021, **27**, 102226.
51 J. Troe, Statistical adiabatic channel model for ion–molecule capture processes. II. Analytical treatment of ion–dipole capture, *J. Chem. Phys.*, 1996, **105**, 6249–6262.
52 A. Haack and W. S. Hopkins, Kinetics in DMS: Modeling Clustering and Declustering Reactions, *J. Am. Soc. Mass Spectrom.*, 2022, **33**, 2250–2262.
53 H. Eyring, The Activated Complex in Chemical Reactions, *J. Chem. Phys.*, 1935, **3**, 107–115.
54 V. Ásgeirsson, B. O. Birgisson, R. Bjornsson, U. Becker, F. Neese, C. Riplinger and H. Jónsson, Nudged Elastic Band Method for Molecular Reactions Using Energy-Weighted Springs Combined with Eigenvector Following, *J. Chem. Theory Comput.*, 2021, **17**, 4929–4945.
55 J. Benny and J. Liu, Spin-orbit charge transfer from guanine and 9-methylguanine radical cations to nitric oxide radicals and the induced triplet-to-singlet intersystem crossing, *J. Chem. Phys.*, 2023, **159**, 085102.
56 L. I. Krishtalik, The mechanism of the proton transfer: an outline, *Biochim. Biophys. Acta, Bioenerg.*, 2000, **1458**, 6–27.
57 A. Haack, C. Schaefer and S. Zimmermann, On the Arrival Time Distribution of Reacting Systems in Ion Mobility Spectrometry, *Anal. Chem.*, 2024, **96**, 12433–12443.
58 J. Troe and V. G. Ushakov, Revisiting falloff curves of thermal unimolecular reactions, *J. Chem. Phys.*, 2011, **135**, 054304.
59 P. Hänggi, P. Talkner and M. Borkovec, Reaction-rate theory: fifty years after Kramers, *Rev. Mod. Phys.*, 1990, **62**, 251–341.
60 G. Bouchoux, J. Y. Salpin and D. Leblanc, A relationship between the kinetics and thermochemistry of proton transfer reactions in the gas phase, *Int. J. Mass Spectrom. Ion Processes*, 1996, **153**, 37–48.
61 K. Sekimoto, S.-M. Li, B. Yuan, A. Koss, M. Coggon, C. Warneke and J. de Gouw, Calculation of the sensitivity of proton-transfer-reaction mass spectrometry (PTR-MS) for organic trace gases using molecular properties, *Int. J. Mass Spectrom.*, 2017, **421**, 71–94.
62 V. S. Langford, K. Dryahina and P. Španěl, Robust Automated SIFT-MS Quantitation of Volatile Compounds in Air Using a Multicomponent Gas Standard, *J. Am. Soc. Mass Spectrom.*, 2023, **34**, 2630–2645.
63 Z. Safaei, T. J. Willy, G. A. Eiceman, J. A. Stone and M. Sillanpää, Quantitative response in ion mobility spectrometry with atmospheric pressure chemical ionization in positive polarity as a function of moisture and temperature, *Anal. Chim. Acta*, 2019, **1092**, 144–150.
64 H. Borsdorf, P. Fiedler and T. Mayer, The effect of humidity on gas sensing with ion mobility spectrometry, *Sens. Actuators, B*, 2015, **218**, 184–190.
65 J. Langejuergen, M. Allers, J. Oermann, A. Kirk and S. Zimmermann, Quantitative detection of benzene in toluene- and xylene-rich atmospheres using high-kinetic-energy ion mobility spectrometry (IMS), *Anal. Chem.*, 2014, **86**, 11841–11846.
66 M. Meot-Ner and C. V. Spellert, Filling of Solvent Shells about Ions. 1. Thermochemical Criteria and the Effects of Isomeric Clusters, *J. Phys. Chem.*, 1986, **90**, 6616–6624.
67 M. Álvarez-Moreno, C. de Graaf, N. López, F. Maseras, J. M. Poblet and C. Bo, Managing the Computational Chemistry Big Data Problem: The ioChem-BD Platform, *J. Chem. Inf. Model.*, 2015, **55**, 95–103.

